


## Article

# Magnetic Resonance Study of Bulky CVD Diamond Disc

Alexander Shames<sup>1</sup>, Alexander Panich<sup>1,\*</sup> , Lonia Friedlander<sup>2</sup>, Haim Cohen<sup>3</sup> , James Butler<sup>4</sup> and Raymond Moreh<sup>1</sup>

<sup>1</sup> Department of Physics, Ben-Gurion University of the Negev, Beer-Sheva 8410501, Israel; sham@bgu.ac.il (A.S.)

<sup>2</sup> Ilse Katz Institute for Nano-Scale Science and Technology, Ben-Gurion University of the Negev, Beer-Sheva 8410501, Israel

<sup>3</sup> Department of Chemical Sciences, Faculty of Exact Science, Ariel University, Ariel 4077625, Israel

<sup>4</sup> Cubic Carbon Ceramics, Huntingtown, MD 20639, USA

\* Correspondence: pan@bgu.ac.il

**Abstract:** Diamonds produced using chemical vapor deposition (CVD) have found many applications in various fields of science and technology. Many applications involve polycrystalline CVD diamond films of micron thicknesses. However, a variety of optical, thermal, mechanical, and radiation sensing applications require more bulky CVD diamond samples. We report the results of a magnetic resonance and structural study of a thick, sizable polycrystalline CVD diamond disc, both as-prepared and treated with e-beam irradiation/high-temperature annealing, as well as gamma irradiation. The combination of various magnetic resonance techniques reveals and enables the attribution of a plentiful collection of paramagnetic defects of doublet and triplet spin origin. Analysis of spectra, electron, and nuclear spin relaxation, as well as nuclear spin diffusion, supports the conclusion of significant macro- and micro-inhomogeneities in the distribution of nitrogen-related defects.

**Keywords:** CVD diamond; electron paramagnetic resonance; nuclear magnetic resonance; paramagnetic defects; defects distribution; spin–lattice relaxation time



**Citation:** Shames, A.; Panich, A.; Friedlander, L.; Cohen, H.; Butler, J.; Moreh, R. Magnetic Resonance Study of Bulky CVD Diamond Disc. *Materials* **2024**, *17*, 1871. <https://doi.org/10.3390/ma17081871>

Academic Editor: Alexander N. Obraztsov

Received: 20 March 2024

Revised: 11 April 2024

Accepted: 15 April 2024

Published: 18 April 2024



**Copyright:** © 2024 by the authors. Licensee MDPI, Basel, Switzerland. This article is an open access article distributed under the terms and conditions of the Creative Commons Attribution (CC BY) license (<https://creativecommons.org/licenses/by/4.0/>).

## 1. Introduction

Chemical vapor deposition (CVD) diamond is a material that has found applications in numerous fields. They include optical applications (infrared windows, lenses, ATR units, X-ray windows), thermal applications (heat spreaders, laser sub mounts, X-ray targets), mechanical applications (cutting tools, scalpels, knives, length gauge tips, wear-resistant components, e.g., for textile machines, inserts for dresser tools), electrochemical applications (electrodes, electrochemical detectors, biochemical sensors), and radiation sensors (ionizing radiation detectors/dosimeters, fluorescence beam monitors). While natural and high pressure–high temperature (HPHT) synthetic diamonds are grown at high pressures under conditions in which diamond is the thermodynamically stable form of crystalline carbon, the growth of CVD diamond occurs at a low pressure in which diamond is not thermodynamically stable, and its growth occurs under highly nonequilibrium conditions [1,2]. Conditions and chemistry of the growth media for CVD diamond are also different from that in which HPHT synthetic diamonds and natural diamonds grow, as CVD diamond is grown at low temperatures and pressures from a mixture of hydrogen and a carbon-containing gas (typically CH<sub>4</sub> or other hydrocarbons) activated by a hot filament, microwave plasma, or other means.

Many important properties of diamonds depend on paramagnetic lattice defects. These defects can result from three basic components, as well as their combinations, including (i) substitutional impurity as the presence of a different atom at a host lattice site, (ii) vacancy as the absence of a host atom at a lattice site, and (iii) interstitial as the presence of a host or impurity atom not at a lattice site. The defects occur during preparation or may be intentionally (or accidentally) introduced by displacing carbon atoms through ionizing

irradiation [3,4] or doping. Even at low concentrations (parts per million, ppm), point defects may significantly affect the properties of diamonds. The abovementioned paramagnetic defects make diamonds show great potential for a variety of applications, particularly,  $NV^-$  centers may work as basic units of a quantum computer and have potential applications in novel electronics and computational science, including quantum cryptography and spintronics [5]. Therefore, the study of these defects is of great importance. The defects can be detected using different types of spectroscopy, including electron paramagnetic resonance (EPR), photoluminescence, cathodoluminescence, and light absorption in the infrared, visible, and ultraviolet parts of the spectrum. Among these, the EPR technique is the most informative.

The first EPR study of CVD diamonds was reported in 1988 [6]. Since that work, both EPR and electron nuclear double resonance (ENDOR) have been extensively used for revealing structure and defects in a variety of CVD diamond syntheses [7–12]. Several paramagnetic defects have been discovered, of which the most common are defects formed by nitrogen impurities, as well as by hydrogen atoms located close to carbon dangling bonds in grain boundaries. The appearance of many defects depends on the preparation procedure and post-processing of samples of CVD diamond. As CVD diamonds are increasingly used in many areas of research and industry, detailed information on the appearance of the defects and their transformations in CVD diamonds remains an important issue.

In many samples grown for both research and applications, relatively thin (up to tens of microns) CVD diamond films are considered [13–24]. In the future, a variety of optical, thermal, mechanical, and radiation sensor applications will require more substantial CVD diamonds [25–32]. It was of certain interest to probe the quality and defect structure of such material. To investigate the properties of such a material at the atomic level, we present in this article the results of EPR, nuclear magnetic resonance (NMR), Fourier transform infrared (FTIR) spectroscopy, and X-ray diffraction (XRD) investigations of a thick, sizable CVD diamond disc. The measurements were carried out using both the as-prepared disc and after e-beam and gamma irradiation, followed by annealing. Detailed investigations of paramagnetic defects have been carried out using a variety of continuous wave (CW) EPR techniques. Several types of primary doublet ( $S = 1/2$ ) and triplet ( $S = 1$ ) defects are revealed, attributed, and quantified. Both EPR and NMR measurements show an inhomogeneous distribution of nitrogen-related defects across the disc at both macro- and micro-levels. NMR data correlate with the EPR results and reveal the nuclear spin diffusion throughout the sample. XRD provides bulk structural information and indicates that the CVD diamond disk contains grains with a distinct preferred growth direction (111).

## 2. Materials and Methods

CVD diamond was deposited from gas-phase mixtures containing hydrogen and methane. The sample was grown in a home-built microwave plasma system made of ASTeX components with a 5 kW microwave source at 2.45 GHz using an HPMM (cylindrical style) chamber, with a water-cooled substrate holder, on a molybdenum substrate (in 1996 at the Naval Research Laboratory). It was approximately 2" in diameter. The final sample was a disc with a diameter of 50 mm and thickness of ca. 560 microns; the plate was delaminated from the substrate on cool down. There were 2 stages to growth, nucleation and then growth. The preparation conditions are recorded in Table 1. Defect/impurity incorporation during growth depends on the local stereochemistry of the growth surfaces, generally, step roughened (100), (111), and (113); (110) apparent surfaces are generally micro-faceted with (111) planes.

**Table 1.** The preparation conditions of the CVD diamond disc.

Stage	Time, h	Pressure, torr	T, °C	Power, W	H <sub>2</sub> , sccm	CH <sub>4</sub> , sccm	O <sub>2</sub> , sccm
Nucleation	60	115	836	4974	500	18	0.5
Growth	56.55	115	836	4974	478	20	2.0

Room temperature (RT,  $T \approx 295$  K) continuous wave (CW) EPR experiments were carried out using a Bruker (Billerica, MA, USA) EMX220 X-band ( $\nu \sim 9.4$  GHz) EPR spectrometer equipped with an Oxford Instrument (Abingdon, UK) ESR900 cryostat and an Agilent (Santa Clara, CA, USA) 53150A frequency counter. Single (10–15 mg weight) and multiple (50–120 mg of total weight) pieces of defragmented large CVD diamond disc were placed in 4 mm o.d. Wilmad EPR quartz tubes and fixed into the Bruker ER 4102ST cavity. Accurate determination of the electronic  $g$ -factors and densities  $N_s$  of primary paramagnetic species within the  $g = 2.00$  region was accomplished by a comparison to a reference sample of highly purified detonation nanodiamond (DND) powder with  $g = 2.0028 \pm 0.0002$  and  $N_s = 6.3 \times 10^{19}$  spins/g or 1255 ppm [33]. The quantification of primary species was carried out as described earlier [34]. Estimation of the triplet centers content and accurate determination of the effective  $g$ -factor for the half-field lines were performed using a comparison of the double-integrated intensities of the half-field ( $g \sim 4.00$  region) EPR lines of all samples under investigation to those for the fluorescent microdiamond sample FMD having  $NV^-$  (W15) content of  $5.4 \times 10^{17}$  spin/g or 10.7 ppm and  $g_{\text{eff}} = 4.272$  (by EasySpin simulation for  $\nu = 9.463$  GHz) [35,36]. Typical experimental error in the determination of spin densities does not exceed 15%.

EPR spectra were registered in two modes, including (a) conventional slow passage (SP) and (b) fast passage (FP) spectra. SP spectra were detected in-phase as the first derivative of the absorption lines using sweep rate  $SR = 0.57$  mT/s and 100 kHz magnetic field modulation amplitude  $A_m = 20$   $\mu$ T for the spectra of primary centers, as well as  $SR = 7.6$  mT/s and  $A_m = 75$   $\mu$ T for the triplet centers. FP spectra of primary centers were detected out-of-phase ( $90^\circ$ ,  $270^\circ$ ) as absorption lines using  $SR = 9.2$  mT/s and  $A_m = 5$   $\mu$ T. Microwave power saturation experiments for primary centers were performed by sweeping the incident microwave power level  $P_{\text{MW}}$  incremented from  $P_{\text{MW}} = 200$  nW (60 dB) to  $P_{\text{MW}} = 200$  mW (0 dB) in 2 dB steps. In situ illumination of the samples was performed through the irradiation grid of the Bruker ER 4102ST cavity with a Fiber-Lite Model 3100 light source (CW, 30 W). EPR data processing and spectral simulation were carried out using Bruker WIN-EPR/SimFonia, EasySpin [36], and OriginLab 7.0 software packages.

For the NMR measurements, similar multiple pieces of defragmented large CVD diamond disk, taken from its two different parts, were used. RT  $^{13}\text{C}$  NMR measurements were carried out using a pulse solid-state NMR spectrometer (Tecmag, Inc., Houston, TX, USA), equipped with a homebuilt NMR probe and an Oxford Instruments wide bore superconducting magnet. The measurements were carried out in a static mode in the external magnetic field  $B_0 = 8.0$  T, corresponding to the  $^{13}\text{C}$  resonance frequency of 85.62 MHz. The  $^{13}\text{C}$  spectra were measured using the Hahn echo pulse sequence  $(\frac{\pi}{2})_x - \tau_d - (\pi)_x$ , and the  $^{13}\text{C}$  spin–lattice relaxation times  $T_{1n}$  were measured using a saturating comb pulse sequence  $(\frac{\pi}{2}$  pulse train). Magnetization recovery in measuring  $T_{1n}$  was fitted by an exponential function. The duration of the  $\frac{\pi}{2}$  pulse was 4.6  $\mu$ s. Data processing and simulations were performed using the OriginLab 7.0 software.

In addition, static RT  $^1\text{H}$  NMR measurements were carried out using the same spectrometer and magnet at the  $^1\text{H}$  resonance frequency of 340.5 MHz. The spectra were measured using the solid echo pulse sequence  $(\frac{\pi}{2})_{0^\circ} - \tau_d - (\frac{\pi}{2})_{90^\circ}$ , a technique that refocuses homonuclear dipole–dipole couplings between protons (here subscripts denote the phases of pulses). The duration of the  $\pi/2$  pulse was 2.2  $\mu$ s.

FTIR spectra analysis in the range of 500–4000  $\text{cm}^{-1}$  were carried out with a Bruker Alpha2 FTIR spectrophotometer, equipped with a ZnSe beam splitter, with a resolution of 2  $\text{cm}^{-1}$ , and collecting 24 scans for each sample. The diamond was placed in a transmittance plug in unit to the FTIR unit. The concentration of the different nitrogen species in the diamonds was calculated using FTIR spectroscopy upon evaluating the C–N bond absorption in the 1000–1400  $\text{cm}^{-1}$  region of the infrared spectrum [37]. Nitrogen concentration was estimated using QUIDDIT program published by Spiech [38].

XRD measurements were conducted at the Ilse Katz Institute for Nano-scale Science and Technology at Ben-Gurion University of the Negev. The measurements were collected

in Bragg–Brentano symmetric ( $\theta/2\theta$ ) geometry using a Panalytical Empyrean III (Malvern Panalytical B.V., Brussels, Belgium) multipurpose diffractometer equipped with a Cu X-ray source ( $K_{\alpha}$  radiation,  $\lambda = 1.541 \text{ \AA}$ ), operated at  $v = 45 \text{ kV}$ ,  $I = 40 \text{ mA}$ . The instrument was further equipped with the iCore–dCore automated XRD optics combination, a pixCEL 3D detector in 1D line-detector mode, and an automated 3-axis eulerian cradle sample stage with control along the z-axis (height) and sample rotation ( $\Phi$ ) and tilt ( $\chi$ ) angles. The CVD diamond sample was measured twice. The first measurement was collected with no sample tilt ( $\chi = 0^{\circ}$ ). The second measurement was collected at a tilt optimized to maximize the intensity of the (220) reflection ( $\chi = 45.76^{\circ}$ ). Collected data were analyzed for phase identification and crystallographic direction by comparison to ideal diamond diffraction patterns found in the International Center for Diffraction Data (ICDD) Powder Diffraction File (PDF-4+) database (2022). The full-width half maximum (FWHM) of relevant reflections were calculated using the Full-Prof Suite Toolbar (version July 2017) to enable the use of the Scherrer formula to estimate crystallite size.

All measurements were performed with as-received samples and those e-beam irradiated with the dose of 1 kGy and gamma-irradiated with the dose of 2 MGy. Irradiated samples were also annealed for 2 h in a vacuum at a temperature of  $850^{\circ}\text{C}$ .

### 3. Results

#### 3.1. XRD Data

The XRD pattern of the investigated CVD diamond (Figure 1) displayed diffraction maxima at the angles  $2\theta = 43.9^{\circ}$  and  $75.2^{\circ}$ , corresponding to the (111) and (220) reflections of a cubic (Fd3m) diamond lattice, respectively (Figure 1). The presence of diffraction peaks from two crystallographic directions suggests a polycrystalline sample because multiple crystallites must be present to meet the Bragg condition in two different orientations from within the sample, which was a solid disc. The initial measurement of the flat ( $\chi = 0^{\circ}$ ) CVD diamond disk shows a relative intensity ratio between the (111) and the (220) reflections that is more than 20 times greater than expected (ideal) for a cubic diamond lattice. The (111) peak intensity suggests greater than micrometer-sized crystallites (calculated Scherrer  $\langle d \rangle > 1220 \text{ nm}$ ) in this growth direction and a strong preferred orientation for the (111) crystallographic plane (Figure 1a). In contrast, the FWHM of the un-tilted ( $\chi = 0^{\circ}$ ) (220) reflection suggests a crystallite  $\langle d \rangle \sim 90 \text{ nm}$ . Optimizing and repeating the XRD measurement oriented around the (220) reflection, returns the relative intensity ratio between the (111) and (220) reflections to the expected range; the (220) reflection is roughly 30% of the (111) intensity (Figure 1b). Maximizing the (220) intensity to optimize sample tilt and eliminate the effects of preferred orientation produces reflections with FWHM values that indicate an overall crystallite size of  $\sim 4 \text{ nm}$ . This suggests that crystallite diameters in the (220) direction range from 4 to 90 nm, significantly smaller than those observed for the preferred (111) direction.

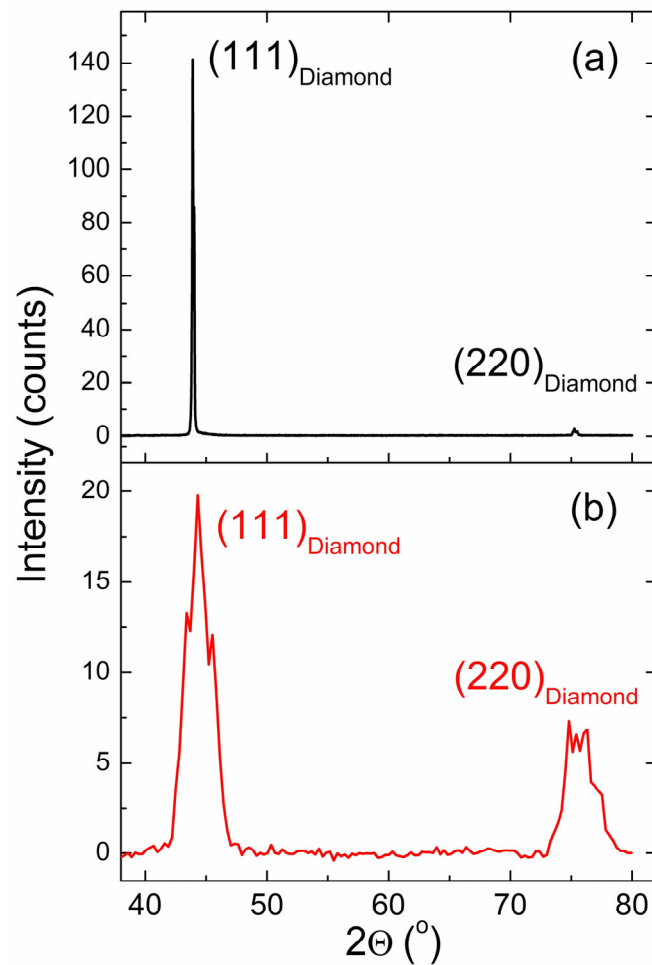


**Figure 1.** Bragg–Brentano geometry reflectance XRD measurements at no tilt (a) and with tilt optimized to maximize the intensity of the (220) reflection (b). The optimized sample tilt in (b) is  $\chi = 45.76^\circ$ .

### 3.2. FTIR Spectra

FTIR spectra (Figure 2) are dominated by phonon absorption bands in the range of  $1500\text{--}2600\text{ cm}^{-1}$ , which are intrinsic to pure diamond. The peaks at  $2800\text{--}3000\text{ cm}^{-1}$  correspond to the stretching vibration of C–H bonds; this finding correlates with the below (Section 3.4) NMR data revealing the proton resonance signal of C–H bonds. A region between  $1500$  and  $1000\text{ cm}^{-1}$  includes the absorption from impurity activated single phonons (nitrogen). The spectra do not show visible changes under irradiation and annealing.

The FTIR spectrum indicates the presence of two types of nitrogen atom impurities in the CVD diamond, including A-centers ( $\text{N}_2$  atoms) and C-centers (single nitrogen atoms). Broad absorption lines do not allow reliable quantitative estimation of each type of nitrogen defects. The total amount of nitrogen in this CVD sample does not exceed 90 ppm.

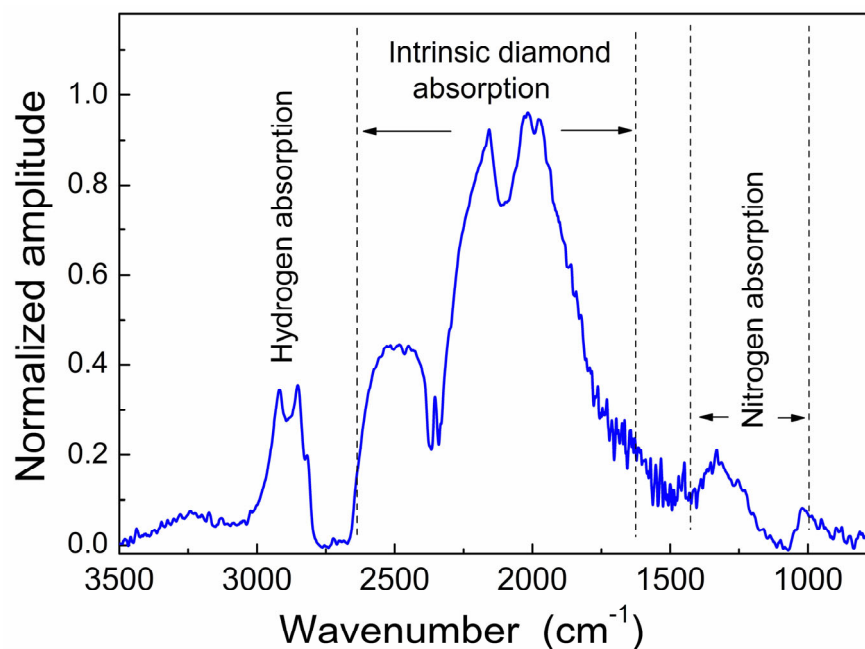


**Figure 2.** Experimental FTIR spectrum of the CVD diamond.

### 3.3. EPR Data

General view RT EPR spectra of all the samples under study consist of a low-intensity broad signal attributed to trace amounts of metallic impurities (further characterization of such impurities falls outside the scope of this study), intense sharp lines within the  $g = 2.00$  region arising from the paramagnetic defects with  $S = 1/2$ , and weak narrow EPR signals observed within in the  $g_{\text{eff}} = 1.8, 2.4,$  and  $4.00$  regions associated with “allowed”  $\Delta M_S = 1$  and “forbidden”  $\Delta M_S = 2$  lines in EPR spectra of triplet ( $S = 1$ ) centers. Because no changes in EPR spectra were revealed in the pieces of the initial CVD sample which had undergone e-beam and gamma irradiation and further high-temperature annealing, the results presented here will describe the untreated (pristine) CVD diamond. EPR spectra of both single and multiple pieces demonstrate the same orientational-independent polycrystalline-like patterns. Because samples consisting of multiple randomly oriented pieces provide higher signal-to-noise ratios (which are extremely important for the reliable registration of weak triplet-related signals) the results presented were collected just on these samples of total weights 50–120 mg.

#### 3.3.1. EPR Spectra of Primary Paramagnetic Centers

Figure 3 shows the  $g = 2.00$  region EPR spectra recorded at two levels of the incident power. SP EPR spectrum observed at low incident power (Figure 3 black trace) clearly demonstrates sharp orientation independent hyperfine triplet pattern, which is characteristic of P1 centers [39,40] overlapped with some broad signals for both central component and satellites. Sharp P1 components start being saturated at  $5 \mu\text{W}$ , whereas other components become saturated at higher power levels. Thus, the spectrum observed at  $200 \mu\text{W}$  (Figure 3, red trace) reveals broad lines around the central ( $m_I = 0$ ) P1 line, as well as broad components around satellite ( $m_I = \pm 1$ ) P1 lines. The non-saturated spectrum (Figure 4, black open circles) may be reasonably simulated as superposition of two  $S = 1/2$  paramagnetic centers, as follows: P1 (single  $^{14}\text{N}$  with  $I = 1$ ,  $g_{\text{iso}} = 2.0024$ ,  $A_{\parallel} = 4.064$  mT,  $A_{\perp} = 2.905$  mT, peak-to-peak Lorentzian line width  $\Delta H_{\text{pp}}(\text{Lorentz}) = 0.018$  mT—see Figure 4, green trace) and a center designated as BS1 (it is generally accepted to designate new paramagnetic defects in diamonds by abbreviations of the laboratory’s location; in this case, BS means Beer-Sheva), characterized by the electronic spin interacting with two  $I = 1$  nuclei ( $g_{\text{iso}} = 2.0028$ ,  $A_{\text{iso}} = 0.08$  mT,  $\Delta H_{\text{pp}}(\text{Lorentz}) = 0.05$  mT—see Figure 3, red trace).

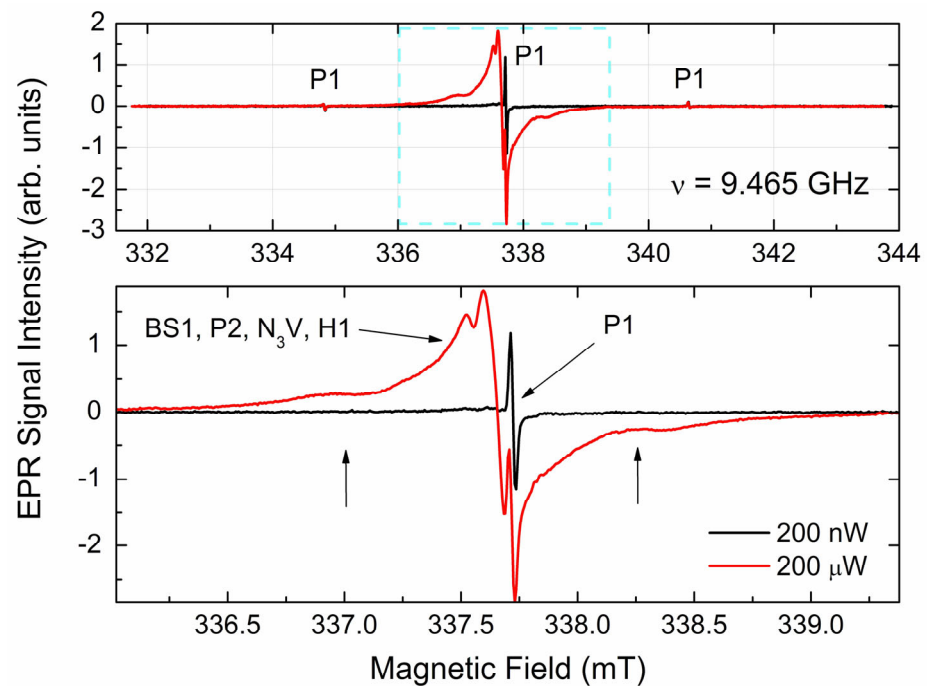


**Figure 3.** RT SP EPR spectra of primary species in the pristine CVD diamond samples. Spectra recorded at  $P_{MW} = 200$  nW (black trace) and  $P_{MW} = 200$   $\mu$ W (red trace),  $SR = 0.57$  mT/s,  $A_m = 20$   $\mu$ T, receiver gain  $RG = 2 \times 10^5$ , and number of coherent acquisitions  $n_{acq} = 100$ ,  $\nu = 9.465$  GHz. Upper panel shows the entire pattern within the  $g = 2.00$  region; sharp triplet indicates P1 centers; lower panel shows zoom of the central line; and arrows point out signatures attributed to various  $S = 1/2$  species (see the text). Vertical arrows point out “forbidden” hyperfine lines in EPR spectra of H1 centers, observed at high  $P_{MW}$  levels.

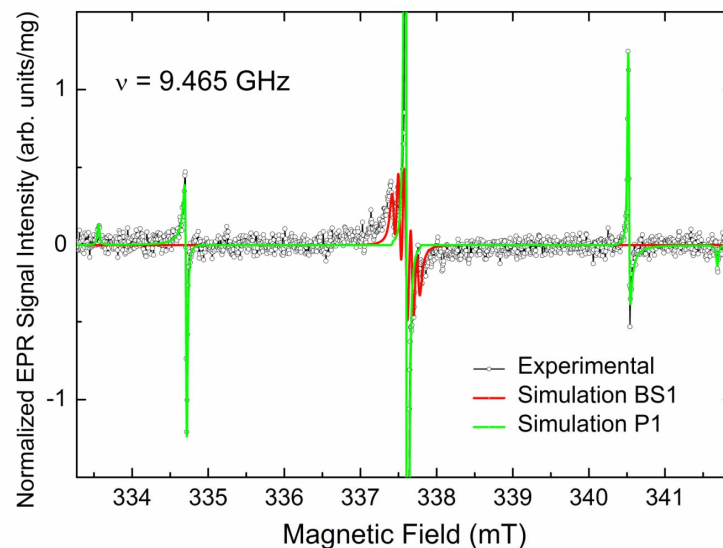


**Figure 4.** Vertical zoom of the RT SP EPR spectrum in Figure 3 recorded at  $P_{MW} = 200$  nW; black open circles—experimental spectrum, red trace—simulated spectrum of BS1, green trace—simulated spectrum of P1. Spin–Hamiltonian parameters used for simulation are listed in the text.

The total content of primary paramagnetic centers, obtained from non-saturated SP EPR spectra was found to be sample-dependent (because different samples originated from different parts of the initial CVD diamond disk) and varies from 2.3 ppm to 4.9 ppm; among these, P1 only content varies from 0.6 ppm to 1.1 ppm.

Further elucidation of the origin of other primary centers was performed using differences in saturation behavior of different primary paramagnetic defects. In fact, defects having longer electronic spin–lattice ( $T_{eSL}$ ) and spin–spin ( $T_{eSS}$ ) relaxation times (like those narrow P1 lines simulated in Figure 4) become saturated at lower microwave power levels, whereas BS1, P2 [39,40], and H1 [6,7,10] centers reveal quite strong signals at much higher power levels—see red traces in Figure 3. Moreover, it is well-known [39] that FP EPR spectra are extremely sensitive to paramagnetic centers having relatively long  $T_{eSL}$ , at which the energy of the electron spin system is exchanged with the environment, and in homogeneously broadened lines [41]. Figure 5 represents the FP EPR spectra of one of the samples under study recorded at incrementing incident power levels.

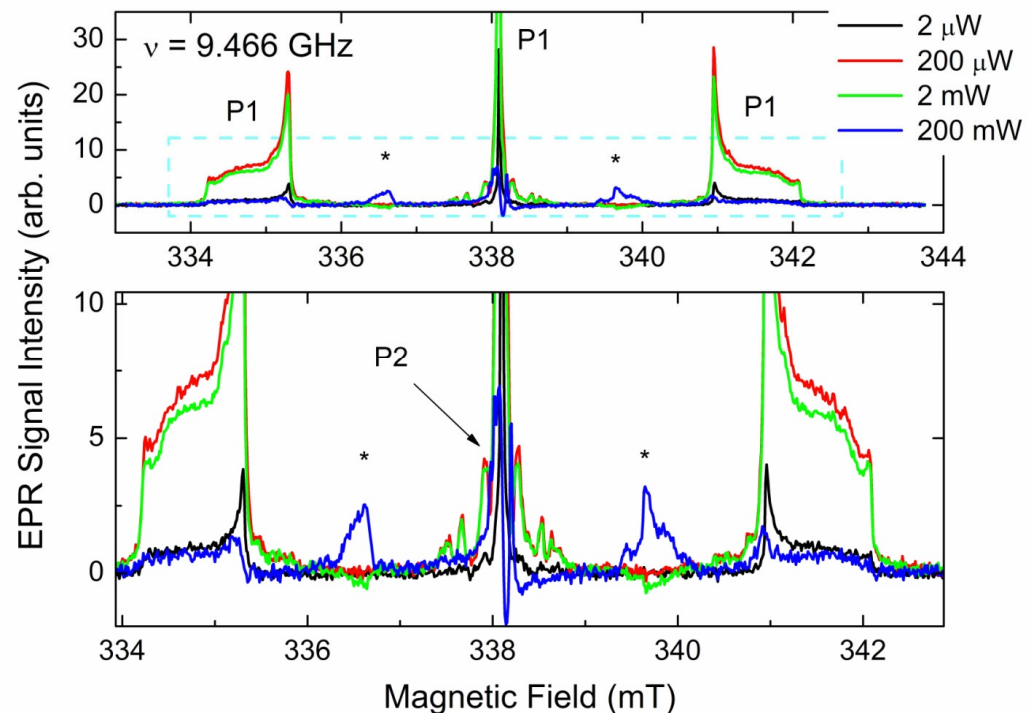


**Figure 5.** RT FP EPR spectra of primary species in the pristine CVD diamond samples. Spectra recorded at  $SR = 9.2$  mT/s,  $A_m = 5$   $\mu$ T,  $RG = 1 \times 10^5$ ,  $n_{acq} = 100$ ,  $\nu = 9.466$  GHz. Spectra were recorded at  $P_{MW} = 2$   $\mu$ W (black trace), 200  $\mu$ W (red trace), 2 mW (green trace), and 200 mW (blue trace). Lower panel shows vertical zoom of satellite lines. Central P1 line is cut for the better presentation of satellite signals. Asterisks point out additional hyperfine satellite lines in between conventional P1 hyperfine components.

Power-dependent FP EPR spectra clearly demonstrate that, in addition to easily saturating narrow P1 components, there are other P1 components that saturate at higher power levels. Some complicated, badly resolved hyperfine patterns on both sides of the central P1 line may be attributed to P2 centers [39,40], which were not observed in SP EPR spectra. Here, it is worth mentioning that FP EPR spectra show no lines that could be attributed to BS1 and H1 centers, which implies that these centers have significantly reduced relaxation times and makes them unobservable in FP detection mode. On the other hand, FP EPR spectra recorded at high power levels ( $P_{MW} > 10$  mW) reveal two additional lines split by  $\sim 3$  mT (asterisks in Figure 5) between the lines of the P1 hyperfine triplet. The origin of these lines will be discussed further.

### 3.3.2. CW EPR Progressive Power Saturation of Primary Centers

Further evidence for the existence of several types of different paramagnetic centers contributing to the central line of CP EPR spectra in Figure 3 was obtained in progressive power saturation experiments. Figure 6 shows the dependence of the peak-to-peak ampli-



tude of the central lines on the incident microwave power (plotted as  $P^{1/2}$ )—saturation curves. The saturation of the narrow line reveals two maxima, including the sharp one characterized by the saturation onset  $5 \mu\text{W}$  and the broad one at the onset of  $\sim 2 \text{ mW}$ . In contrast, the saturation curve for the broad line demonstrates saturation onset at  $\sim 50 \text{ mW}$ . Thus, the narrow line consists of two components, including very fast and moderate saturating ones. Both these components become totally saturated at  $P_{\text{MW}} \geq 20 \text{ mW}$  and, therefore, unobservable. On the other hand, the broad line reveals a single component saturating at a noticeably higher power level. Analysis of the saturation curves' behavior [42,43] allows for the estimation of  $T_{\text{eSL}}$  values for each of the components described above—see solid and dashed lines in Figure 6 representing best least square fits. Thus, paramagnetic centers responsible for the narrow line may be characterized by  $T_{\text{eSL1}} \sim 230 \mu\text{s}$  and  $T_{\text{eSL2}} \sim 1.6 \mu\text{s}$ , whereas the broad line reveals  $T_{\text{eSL}} \sim 0.21 \mu\text{s}$ .

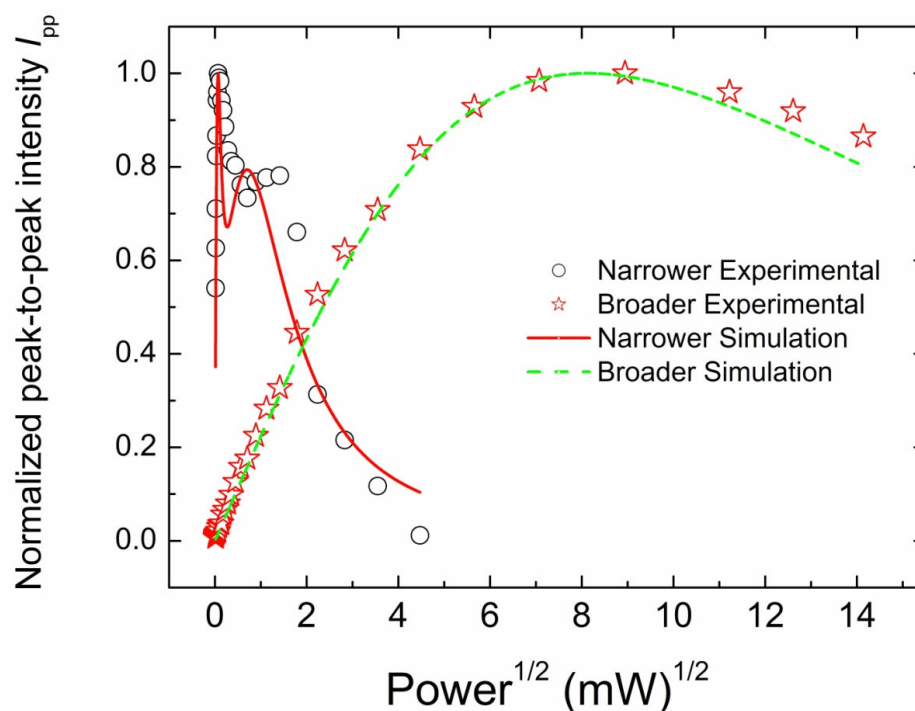


**Figure 6.** Peak-to-peak amplitudes of the central ( $g = 2.00$ ) lines in the X-band SP EPR spectra of CVD diamond sample as a function of the incident microwave power (saturation curves); black open circles—narrow line, and red open stars—broad line. Line traces demonstrate best least square fits; red solid line—double component fit for the narrow line, green dashed line—single component fit for the broad line. At  $P_{\text{MW}} \geq 20 \text{ mW}$  the narrow line becomes totally unobservable.

### 3.3.3. EPR Spectra of Triplet ( $S = 1$ ) Paramagnetic Centers

In addition to the intensive signals within the  $g = 2.00$  region, SP EPR spectra reveal a set of weak sharp signals within the half-field region  $g_{\text{eff}} = 4.00$ , as well as low- and high-fielded satellites to the primary signals located at  $g_{\text{eff}} = 2.4$  and  $1.8$ , correspondingly. Figure 7 shows the half-field signal of the CVD diamond sample (black trace) in comparison with the half-fielded signals in the reference FMD (red trace) and DND (green trace) samples.

The only EPR signal observed in the  $g = 4$  region for the initial CVD diamond sample is a low-intensity asymmetric narrow ( $\Delta H_{\text{pp}} = 0.15 \text{ mT}$ ) line located at  $g_{\text{eff}} = 4.241 \pm 0.005$ . This line is attributed to “forbidden”  $\Delta M_S = 2$  lines in EPR spectra of triplet ( $S = 1$ ) center designated as BS2. The intensity of the “forbidden” line in the pristine CVD sample is found to be sample-dependent. Thus, the content of the triplet centers responsible for this line varies between pieces from  $\sim 9 \text{ ppb}$  to  $\sim 30 \text{ ppb}$ . Saturation onset for these centers is at  $\sim 20 \text{ mW}$ , and the spin–lattice relaxation time was estimated as  $T_{\text{eSL}}^{\text{forbidden}} \sim 0.32 \mu\text{s}$ . The

half-field line is accompanied by the same weak narrow lines located on both sides of the primary signals' region (Figure 8). These lines in the polycrystalline EPR pattern of triplets correspond to the "allowed"  $x$ -,  $y$ - transitions between Zeeman sublevels. Distance between these low- and high-field lines allows direct determination of zero field splitting  $D$ , which is found to be  $D = 0.0908 \pm 0.0001 \text{ cm}^{-1}$ . EasySpin simulation of the polycrystalline pattern using  $g_{\text{iso}} = 2.0024$  and  $D = 0.0908 \text{ cm}^{-1}$  provides for the "forbidden" line  $g_{\text{eff}} = 4.240$ , which is in good agreement with the experimentally found value. Attempts to register both the half-field and satellite lines in the FP EPR mode were unsuccessful.

Here, it is worth mentioning that in situ illumination of the CVD samples using white light causes no changes in intensities of "forbidden" and "allowed" lines associated with the BS2 triplet center.

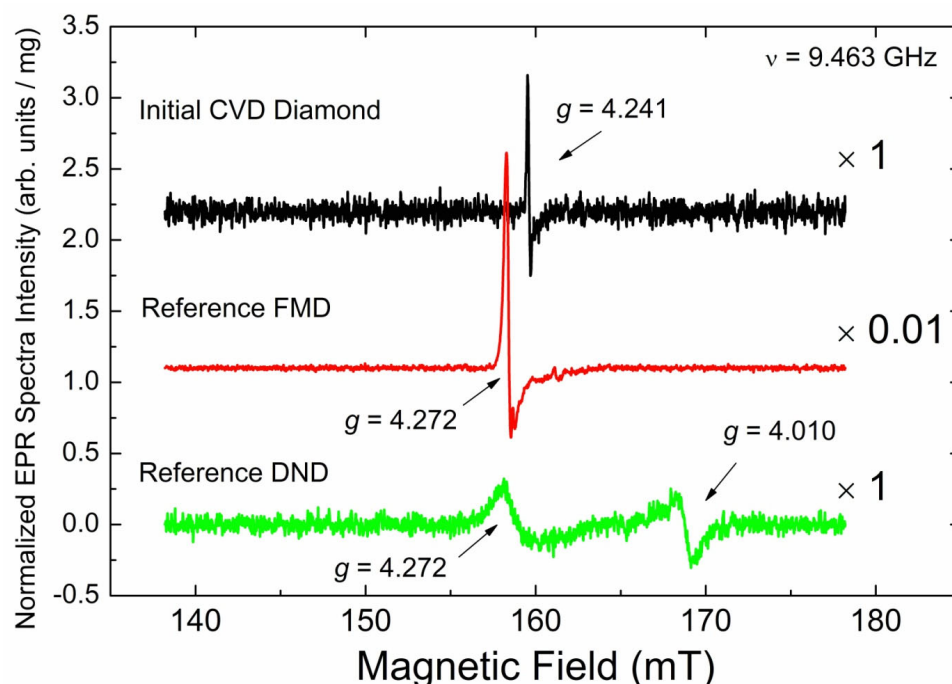


**Figure 7.** Half-field RT SP EPR spectra ( $g = 4.00$  region); black trace—initial CVD diamond pieces, red trace—reference FMD sample, green trace—reference DND sample. Arrows mark effective  $g$ -factors for the "forbidden" lines with  $g_{\text{eff}} = 4.241 \pm 0.005$  (CVD),  $g_{\text{eff}} = 4.272$  (FMD, DND) and  $g_{\text{eff}} = 4.010$  (DND). Spectra recorded at  $\text{SR} = 7.6 \text{ mT/s}$ , non-saturating power levels  $P_{\text{MW}} = 5 \text{ mW}$  (CVD, DND), and  $P_{\text{MW}} = 50 \text{ }\mu\text{W}$  (FMD),  $A_{\text{m}} = 0.075 \text{ mT}$  (CVD, FMD) and  $A_{\text{m}} = 0.75 \text{ mT}$  (DND),  $\text{RG} = 2 \times 10^6$ ,  $n_{\text{acq}} = 400$ ,  $\nu = 9.463 \text{ GHz}$ . Intensities of the spectra were normalized per unit mass and the uniform setup; scaling factors are shown on the right. Background signals have been subtracted.

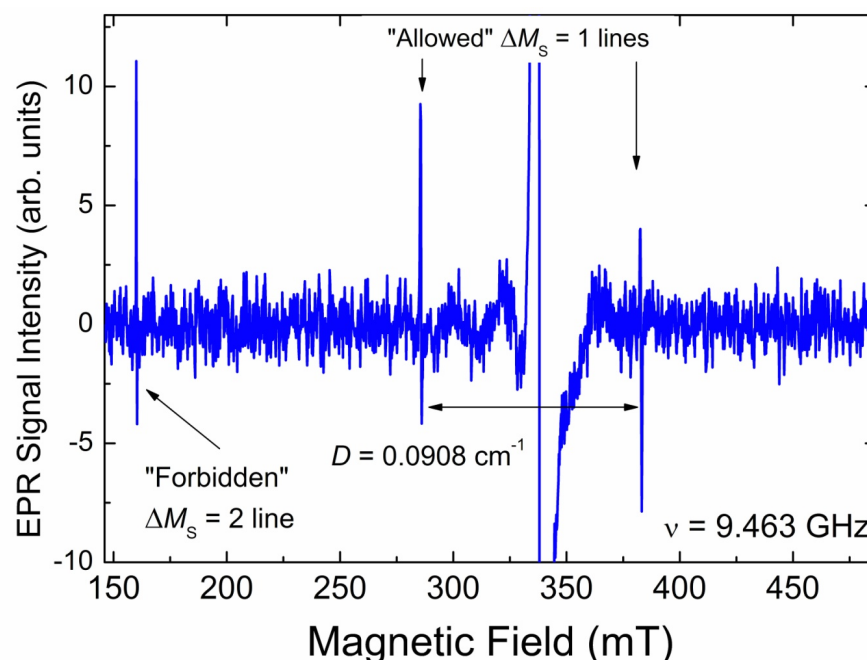


**Figure 8.** All triplet-related lines (both “forbidden” at half-field and “allowed” on both sides of the intense  $g = 2.00$  signals, marked by arrows) in the SP EPR spectrum of the CVD diamond sample. Spectrum was recorded at  $SR = 19$  mT/s,  $P_{MW} = 2$  mW,  $A_m = 0.3$  mT, and  $RG = 2 \times 10^6$  central signals, with  $g = 2.00$  are omitted for clarity. Background signal has been subtracted. Intense  $g = 2.00$  line is cut for better presentation of weaker triplet-related lines.

### 3.4. NMR Study of CVD Diamond

$^{13}\text{C}$  NMR spectra of bulky CVD diamond disc pieces and, for comparison, of the powder of 5 nm DNDs are shown in Figure 9. One can see that these spectra are quite different. The DND particle consists of a diamond core and a partially disordered shell with a hydrogen-terminated surface [44–47]. This is reflected in the  $^{13}\text{C}$  spectrum of DNDs, which is deconvoluted into two components (Figure 9). Our CVD diamond reveals a single  $^{13}\text{C}$  line, which is much narrower than that in DNDs, meaning a more ordered structure compared to DNDs, and no visible signal of a disordered shell.

Let us now discuss nuclear spin–lattice relaxation characterized by a time  $T_{1n}$ , at which the energy of the spin system is exchanged with the environment. In the absence of motions with a relatively narrow frequency distribution, such as molecular reorientations, nuclear spin–lattice relaxation in a diamagnetic system occurs due to lattice vibrations that cause energy exchange between the nuclear spin system and lattice phonons. Because the nuclear transition frequencies are small compared to the lattice vibration frequencies, the phonon density at the resonance frequencies is too small to be effective in the nuclear spin–lattice relaxation. The Raman process, in which the difference between the incoming and outgoing phonon frequencies is on the order of NMR frequency, can involve more phonons but is also not effective enough. Therefore, the  $^{13}\text{C}$  spin–lattice relaxation process in gem diamonds may last from several hours to days. However, the spin–lattice relaxation noticeably accelerates in the case of nuclear relaxation via unpaired electron spins of localized paramagnetic defects due to the strong electron–nuclear interaction and effective heat contact of the electron spins with the lattice modes, which produce an effective channel for the nuclear spin–lattice relaxation. Herewith, according to the theory [48,49], nuclear spin–lattice relaxation time  $T_{1n}$  is inversely proportional to the density of paramagnetic defects  $N_S$ . This is the case with our  $^{13}\text{C}$  NMR measurements, which show a decrease in relaxation time with an increased number of paramagnetic defects detected by EPR (see Table 2 and Figure 10). While some pieces of our initial CVD diamond with  $N_S \sim 3$  ppm show  $T_{1n} = 2070$  s, the relaxation time in the pieces taken from the other location of the

CVD diamond disc with  $N_S \sim 5$  ppm of defects is 1.54 times shorter,  $T_{1n} = 1340$  s (Table 2 and Figure 10).

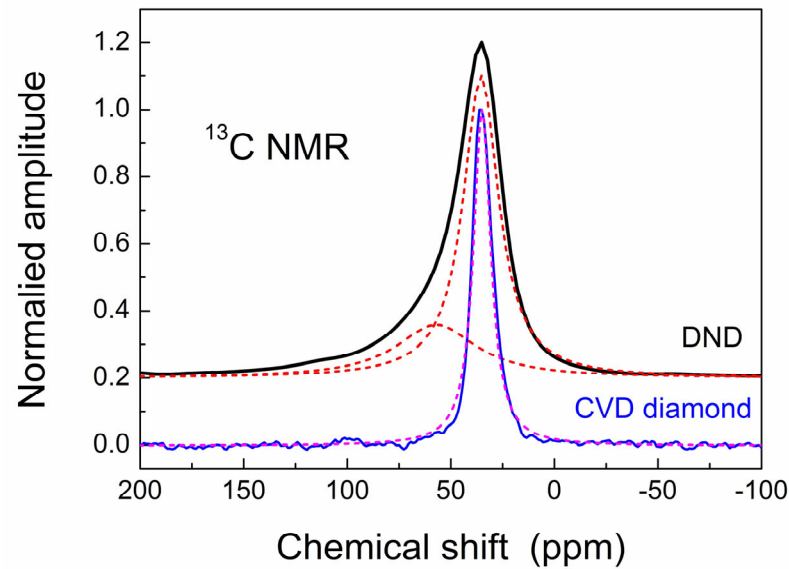


**Figure 9.** Comparative  $^{13}\text{C}$  spectra of powdered DND sample and CVD diamond disc. The DND spectrum is deconvoluted into two components. Red and wine dashed lines show Lorentzian fits.

**Table 2.** The density of paramagnetic defects  $N_S$  and spin–lattice relaxation times  $T_{1n}$  in two different parts of the CVD diamond disc CVD-1 and CVD-2.

Sample	$N_S$ , ppm	$T_{1n}$ , s
CVD-1	3	$2070 \pm 79$
CVD-2	5	$1340 \pm 126$

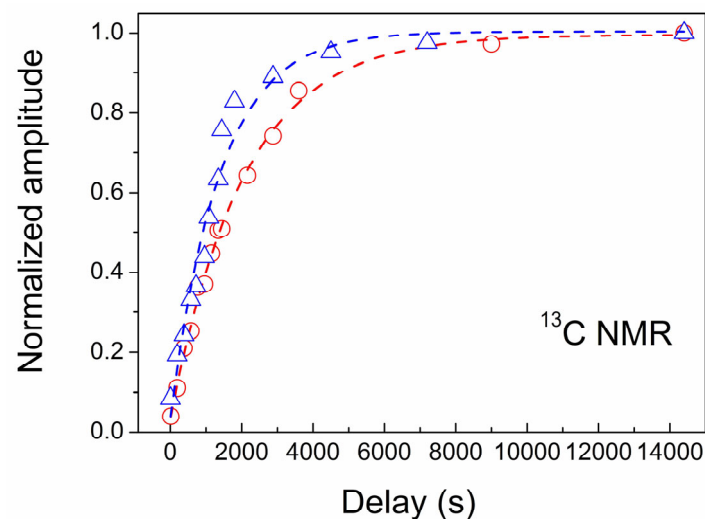


**Figure 10.**  $^{13}\text{C}$  magnetization recovery of two different samples taken from the same CVD diamond disc shown by red circles ( $N_S \sim 3$  ppm) and blue triangles ( $N_S \sim 5$  ppm). Dashed lines show theoretical fits.

We note that nanodiamonds with  $N_S = 6.3 \times 10^{19}$  spin/g, or 1256 ppm, show  $^{13}\text{C}$  spin–lattice relaxation time  $T_{1n}$  around half a second [44–47,50–53].

When a CVD diamond is deposited from gas-phase mixtures containing hydrogen and methane, its surface is somewhat terminated by hydrogen, forming C–H bonds. In the CVD

films, such bonds were previously detected by infrared and NMR spectroscopies [54,55]. Therefore, in addition to the  $^{13}\text{C}$  NMR measurements discussed above, we also measured the proton magnetic resonance spectrum to check whether such an effect appears in our sample. The result is that our CVD diamond reveals a very weak hydrogen signal (Figure 11) attributed to the surface C–H bonds. This assumes that the hydrogen atoms are not incorporated into the diamond core but are located in grain boundaries and interact with the carbon dangling bonds. This finding is in agreement with the EPR data on the H1 centers.

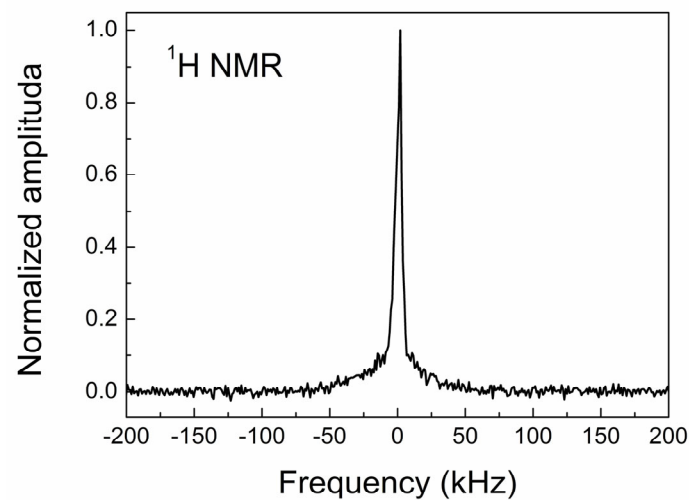


**Figure 11.** Proton magnetic resonance spectrum of CVD diamond.

#### 4. Discussion

FTIR data indicate the presence of a certain amount (~90 ppm) of nitrogen defects, among them nonparamagnetic aggregated nitrogen pairs (A-centers) and paramagnetic substitutional nitrogen (C-centers, or P1). The combination of CW EPR spectra recorded in both SP and FP modes and progressive power saturation experiments reveals that this bulk CVD diamond sample is rich in various paramagnetic defects. The main paramagnetic species in this sample is substitutional nitrogen  $N_s$  (P1 centers), which is found to be strongly inhomogeneously distributed over the CVD diamond volume. Moreover, the observed inhomogeneity exists at both macroscopic and microscopic levels. The former is indicated by variations of the P1 (and other primary defects) content between the samples taken from different parts of the bulk CVD diamond disk. The latter becomes clear from the analysis of the saturation behavior of P1-related spectra. Thus, there are at least three kinds of P1 centers distinguished by line width and relaxation behavior, including (i) well-isolated P1 centers responsible for the narrow slow relaxing components in polycrystalline EPR patterns; (ii) clusterized P1 centers responsible for broader faster relaxing components, better observed in FP spectra recorded at higher  $P_{MW}$  levels (see red and green traces in Figure 4), and (iii) exchange-coupled P1 pairs responsible for the additional hyperfine components with half splitting  $A \sim 1.5$  mT (marked by asterisks on the blue trace in Figure 5) [56,57]. A forcible argument in favor of the hypothesis on the inhomogeneous distribution of P1 centers may be drawn from the careful analysis of the line width and shape of the central ( $m_I = 0$ ) line of the P1 triplet pattern. The experimental line width for this line was found to be  $\Delta H_{pp} = 0.018$  mT. Supposing the origin of this line is determined by dipole–dipole interaction between P1 centers and, following the van Wyk model [58], one can predict a line width of ~0.012 mT for the P1 content range 0.6–1.1 ppm found in the sample under study. The line width found (0.018 mT) corresponds to the P1 content above 13 ppm. The latter is higher than the total content of all primary centers in this sample, which does not exceed 5 ppm. Black open circles in Figure 12 represent the high-resolution SP EPR spectrum of the central line. It is clearly seen that the line is slightly asymmetric and most probably consists of two lines differing by their  $g$ -factors and line widths. The experimental spectrum

may be successfully simulated by two overlapping Lorentzian-shaped components (red trace) shifted by  $\Delta g \sim 0.00005$  and having  $\Delta H_{pp} = 0.008$  mT (green trace) and  $0.011$  mT (blue trace), correspondingly. These components may be attributed to slow-relaxing P1 species distinguished by the density of P1 spins in their neighborhood.

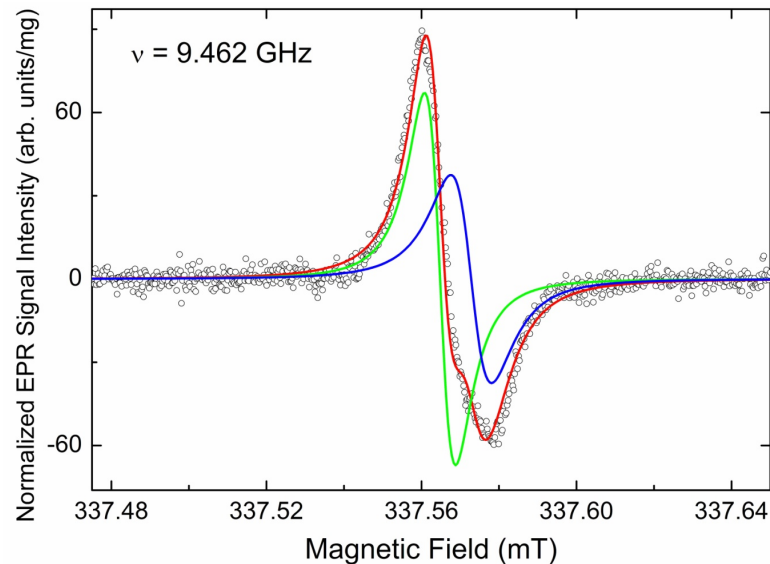


**Figure 12.** High-resolution RT SP EPR spectrum (open black circles) of the central ( $m_l = 0$ ) line in the pristine CVD diamond samples. Spectrum recorded at  $P_{MW} = 200$  nW, SR = 0.0477 mT/s,  $A_m = 2$   $\mu$ T, receiver gain RG =  $1 \times 10^6$ , and number of coherent acquisitions  $n_{acq} = 100$ ,  $\nu = 9.462$  GHz. Red trace shows best least square fit of the experimental spectrum using two Lorentzian components, including narrower  $\Delta H_{pp} = 0.008$  mT (green trace) and broader  $\Delta H_{pp} = 0.011$  mT (blue trace).

In addition to P1 centers, some other nitrogen-related paramagnetic centers were found. Among these, P2 [39,40] and N3V [59] centers may be identified as relatively slow relaxing; in addition, BS1 centers have even shorter relaxation times and are thus unobservable in the FP EPR mode. A small (0.08 mT) nitrogen hyperfine splitting constant found for the BS1 centers points out the interaction of the uncoupled electronic spin (most probably due to vacancy) interacting with the nuclei of two distant nitrogen atoms. None of the previously reported dinitrogen paramagnetic defects (like N1, N4, and W7) satisfy the observation of such a small  $^{14}\text{N}$  hyperfine constant [39,40]. It allows for the speculation that such a defect has not been previously reported. SP ERP spectra recorded at higher power levels reveal also traces of a slow saturating doublet split by  $\Delta H \sim 1.3$  mT, (see red trace in Figure 3 and arrows in the zoom panel). These hardly saturating satellite lines may be reliably attributed to “forbidden” hyperfine transitions ( $\Delta m_l = \pm 1$ ) in the EPR spectra of H1 centers, which are carbon dangling bonds interacting with hydrogen atoms located in grain boundaries [7].

In an attempt to identify the triplet center BS2, its Spin–Hamiltonian parameters ( $g$ ,  $D$ ) were compared to the same parameters known for a variety of triplet defects previously observed in diamonds [40]. The best match has been found for the W27 triplet center with  $g_{iso} = 2.0025$  and  $D = +1794$  MHz, which corresponds to  $D = 0.0898$   $\text{cm}^{-1}$ . W27 had been observed in green natural type Ia diamonds and was associated with some nitrogen clusters [60]. In fact, the difference in  $D$ -values for BS2 ( $0.0908$   $\text{cm}^{-1}$ ) and W27 ( $0.0898$   $\text{cm}^{-1}$ ) exceeds the experimental error in  $D$ -determination ( $0.0001$   $\text{cm}^{-1}$ ). The same concerns the  $g_{eff}$ -values for the “forbidden” line, which is  $g_{eff} = 4.241$  for BS2 and  $g_{eff} = 4.239$  for W27 (by EasySpin simulation). These differences allow for the speculation that BS2 is not exactly the same center as W27. On the other hand, the association of BS2 with some nitrogen clusters does make sense, especially taking into account the strongly inhomogeneous distribution of nitrogen-related defects claimed above.

It is important to note that our EPR study revealed no traces of  $NV^-$  (W15) centers in the CVD diamond sample under study. Moreover, low-fluence e-beam irradiation/annealing and high-fluence gamma irradiation did not create new centers in that nitrogen-containing diamond structure. This strange fact requires further e-beam irradiation/annealing treatment followed by a thorough fluorescent and optically detected magnetic resonance (ODMR) study.

The abovementioned inhomogeneous distribution of the paramagnetic centers over the CVD diamond volume is well-supported by NMR measurements, showing different nuclear spin–lattice relaxation times in two samples taken from different parts of the bulky CVD diamond disc. Herewith the values of the measured relaxation times correlate with the number of paramagnetic centers in these parts measured by EPR.

Let us now discuss the nuclear spin–lattice relaxation in more detail. As shown by Abragam [48] and Goldman [49], nuclear spin–lattice relaxation in solids is mainly caused by the dipole–dipole interaction of nuclear spins with electron spins of paramagnetic defects. Taking into account the dipolar coupling is a short-range interaction and that the concentration of paramagnetic defects in the studied CVD diamond is small (only several ppm), one should explain the nuclear spin–lattice relaxation between the electron spins and distant nuclei. This was performed by Bloembergen [61], who proposed that spin magnetization in a rigid lattice is spatially transferred by nuclear spin diffusion. This mechanism occurs through the mutual flips of neighboring nuclear spins due to interaction terms of  $I_i^+ I_j^-$  type and results in the magnetization transfer from the distant nuclear spins to the localized electron spins. Reynhardt and Hoch [62,63] showed that spin diffusion dominates  $^{13}C$  spin–lattice relaxation in diamonds at  $N_S < 10$  ppm, which is just the case in the question of our samples. Taking into account that the  $^{13}C$  spins with natural abundance  $n_c = 1.07\%$  are distributed in a random way in the lattice, and using Poisson distribution by putting the probability, they calculated a typical distance  $r_{C-C}$  between two carbon spins as  $r = 0.55n_c^{-1/3} = 4.42 \text{ \AA}$  and the  $^{13}C$  nuclei spin diffusion coefficient as  $D \approx 7.6 \times 10^{-14} \text{ cm}^2 \text{ s}^{-1}$  [63]. The distance over which the spin diffusion can operate is  $L = \sqrt{2DT_1}$ , yielding  $L = 1774 \text{ \AA}$  for  $T_{1n} = 2070 \text{ s}$ . Being applied to the CVD diamond under study, the same approach yields a distance between the paramagnetic defects as 57 and 67.6  $\text{ \AA}$  for  $N_S = 5$  and 3 ppm, respectively. Thus, spin diffusion can transfer magnetization throughout the  $^{13}C$  spin system and induce nuclear spin–lattice relaxation via paramagnetic defects.

## 5. Conclusions

We studied the spectroscopic and structural properties of a thick, sizable CVD diamond disc using EPR, NMR, FTIR, and XRD techniques. The measurements of the as-prepared disc and that after electron and gamma irradiation have been carried out. Detailed investigations of paramagnetic defects have been conducted using a variety of CW EPR techniques. EPR and NMR measurements vote for significantly inhomogeneous distribution of defects across the disk at both macroscopic and microscopic levels. NMR data correlate with the EPR data and reveal nuclear spin diffusion throughout the sample.

**Author Contributions:** Conceptualization, A.S., A.P. and R.M.; methodology, A.S., A.P., H.C. and J.B.; investigation, A.S., A.P., L.F. and H.C.; resources, J.B.; data curation, A.S. and A.P.; writing—original draft preparation, A.S., A.P. and L.F.; writing—review and editing, A.S., A.P., L.F. and J.B.; supervision, R.M.; project administration, R.M.; funding acquisition, R.M. All authors have read and agreed to the published version of the manuscript.

**Funding:** This research received no external funding.

**Institutional Review Board Statement:** Not applicable.

**Informed Consent Statement:** Not applicable.

**Data Availability Statement:** Data are contained within the article.

**Conflicts of Interest:** Author James Butler was employed by the company Cubic Carbon Ceramics. The remaining authors declare that the research was conducted in the absence of any commercial or financial relationships that could be construed as a potential conflict of interest.

## References

1. Goodwin, D.G.; Butler, J.E. *Handbook of Industrial Diamonds and Diamond Films*; Prelas, M.A., Popovici, G., Biglow, L.K., Eds.; Marcel Dekker, Inc.: New York, NY, USA, 1997; pp. 527–581.
2. D’Haenens-Johansson, U.F.S.; Butler, J.E.; Katrussha, A.N. Synthesis of Diamonds and Their Identification. *Rev. Mineral. Geochem.* **2022**, *88*, 689–754. [[CrossRef](#)]
3. Shames, A.I.; Panich, A.M.; Kempinski, W.; Baidakova, M.V.; Osipov, V.Y.; Enoki, T.; Vul’, A.Y. Magnetic resonance study of nanodiamonds. In *Synthesis, Properties and Applications of Ultrananocrystalline Diamond*; Gruen, D.M., Shenderova, O.A., Vul, A.Y., Eds.; NATO Science Series, Series II: Mathematics, Physics and Chemistry; Springer: Berlin/Heidelberg, Germany, 2005; Volume 192, pp. 271–282. Available online: [https://books.google.co.il/books/about/Synthesis\\_Properties\\_and\\_Applications\\_of.html?id=gV5Nqsbr-ugC&redir\\_esc=y](https://books.google.co.il/books/about/Synthesis_Properties_and_Applications_of.html?id=gV5Nqsbr-ugC&redir_esc=y) (accessed on 17 April 2024).
4. Arnault, J.-C. (Ed.) *Nanodiamonds: Advanced Material Analysis, Properties and Applications*; Elsevier: Amsterdam, The Netherlands, 2017; 488p. Available online: <https://www.elsevier.com/books/nanodiamonds/arnault/978-0-323-43029-6> (accessed on 17 April 2024).
5. Wrachtrup, J.; Jelezko, F. Processing Quantum Information in Diamond. *J. Phys. Condens. Matter* **2006**, *18*, S807–S824. [[CrossRef](#)]
6. Watanabe, I.; Sugato, K. EPR in diamond thin films synthesized by microwave plasma chemical vapor deposition. *Jpn. J. Appl. Phys.* **1988**, *27*, 1808–1811. [[CrossRef](#)]
7. Zhou, X.; Watkins, G.D.; Mcnamara-Rutledge, K.M.; Messmer, R.P.; Chawla, S. Hydrogen-related defects in polycrystalline CVD diamond. *Phys. Rev. B* **1996**, *54*, 7881–7890. [[CrossRef](#)]
8. Rohrer, E.; Graeff, C.F.O.; Janssen, R.; Nebel, C.E.; Stutzmann, M.; Guttler, H.; Zachai, R. Nitrogen-related dopant and defect states in CVD diamond. *Phys. Rev. B* **1996**, *54*, 7874–7880. [[CrossRef](#)] [[PubMed](#)]
9. Lukins, P.B.; Khachan, J. Power saturation and the effect of argon on the electron spin resonance of diamond deposited from a microwave plasma. *Appl. Phys. Lett.* **1994**, *65*, 3320–3322. [[CrossRef](#)]
10. Talbot-Ponsonby, D. Paramagnetic Defects in CVD Diamonds. Ph.D. Thesis, University of Oxford, Oxford, UK, 1997.
11. Hartland, C.B. A Study of Point Defects in CVD Diamond Using Electron Paramagnetic Resonance and Optical Spectroscopy. Ph.D. Thesis, University of Warwick, Coventry, UK, 2014.
12. Ashfold, M.N.R.; Goss, J.P.; Green, B.L.; May, P.W.; Newton, M.E.; Peaker, C.V. Nitrogen in diamond. *Chem. Rev.* **2020**, *120*, 5745–5794. [[CrossRef](#)]
13. May, P.W. Diamond thin films: A 21st-century material. *Phil. Trans. R. Soc. Lond. A* **2000**, *358*, 473–495. [[CrossRef](#)]
14. Buijnsters, J.G.; Shankar, P.; van Enckevort, W.J.P.; Schermerd, J.J.; Meulen, J.J.T. Adhesion analysis of polycrystalline diamond films on molybdenum by means of scratch, indentation and sand abrasion testing. *Thin Solid Films* **2005**, *474*, 186–196. [[CrossRef](#)]
15. Kim, J.H.; Lee, S.K.; Kwon, O.M.; Lim, D.S. Ultra Thin CVD Diamond Film Deposition by Electrostatic Self-Assembly Seeding Process with Nano-Diamond Particles. *J. Nanosci. Nanotechnol.* **2009**, *9*, 4121. [[CrossRef](#)]
16. Salenbien, R.; Sermeus, J.; Pobedinskas, P. Christ Glorieux<sup>1</sup>, Ken Haenen. Thin Nano- and Microcrystalline CVD Diamond Films for Micro-channel Cooling: Thermal and Elastic Properties. *MRS Online Proc. Libr.* **2010**, *1282*, 1502.
17. Nemanich, R.J.; Carlisle, J.A.; Hirata, A.; Haenen, K. CVD diamond—Research, applications, and challenges. *MRS Bulletin* **2014**, *39*, 490. [[CrossRef](#)]
18. Nistor, P.A.; May, P.W. Diamond thin films: Giving biomedical applications a new shine. *J. R. Soc. Interface* **2017**, *14*, 20170382. [[CrossRef](#)] [[PubMed](#)]
19. Kratochvilova, I. Polycrystalline Diamond Thin Films for Advanced Applications. In *Advances in Carbon Nanostructures*; Silva, A.M.T., Carabineiro, S.A.C., Eds.; IntechOpen: London, UK, 2016; Chapter 8, pp. 161–173. Available online: <https://www.intechopen.com/chapters/51835> (accessed on 17 April 2024).
20. Polushin, N.I.; Laptev, A.I.; Spitsyn, B.V.; Alexenko, A.E.; Polyansky, A.M.; Maslov, A.L.; Martynova, T.V. Deposition of Boron-Doped Thin CVD Diamond Films from Methane-Triethyl Borate-Hydrogen Gas Mixture. *Processes* **2020**, *8*, 666. [[CrossRef](#)]
21. Salvatori, S.; Pettinato, S.; Piccardi, A.; Sedov, V.; Voronin, A.; Ralchenko, V. Thin Diamond Film on Silicon Substrates for Pressure Sensor Fabrication. *Materials* **2020**, *13*, 3697. [[CrossRef](#)] [[PubMed](#)]
22. Wei, S.; Xie, R.; Li, Y.; Meng, J.; Lin, R.; Weng, J.; Li, B. Deposition of diamond films by microwave plasma CVD on 4H-SiC Substrates. *Mater. Res. Express* **2023**, *10*, 126404. [[CrossRef](#)]
23. Haddad, M.; Kurtulus, O.; Mertens, M.; Brühne, K.; Glüche, P.; Fecht, H. Optimization of residual stresses inside diamond thin films grown by hot filament chemical vapor deposition (HFCVD). *Diamond Relat. Mater.* **2023**, *131*, 109564. [[CrossRef](#)]
24. Martynov, A.; Tiazhelov, I.; Savin, S.; Voronov, V.; Konov, V.; Sedov, V. Synthesis of Polycrystalline Diamond Films in Microwave Plasma at Ultrahigh Concentrations of Methane. *Coatings* **2023**, *13*, 751. [[CrossRef](#)]
25. Guo, X.; You, Y.; Bao, A.; Jia, P.; Xiong, J.; Li, J. Recent Progress of Nanodiamond Film in Controllable Fabrication and Field Emission Properties. *Nanomaterials* **2023**, *13*, 577. [[CrossRef](#)]
26. Feng, M.; Jin, P.; Meng, X.; Xu, P.; Wu, J.; Wang, Z. One-step growth of a nearly 2 mm thick CVD single crystal diamond with an enlarged surface by optimizing the substrate holder structure. *J. Cryst. Growth* **2023**, *603*, 127011. [[CrossRef](#)]



27. Hu, X.; Li, M.; Wang, Y.; Peng, Y.; Tang, G.; Wang, X.; Li, B.; Yang, Y.; Xu, M.; Xu, X.; et al. Growth of 2-inch diamond films on 4H-SiC substrate by microwave plasma CVD for enhanced thermal performance. *Vacuum* **2023**, *211*, 111895. [[CrossRef](#)]
28. Liang, Y.; Liu, K.; Liu, B.; Li, Y.; Fan, S.; Dai, B.; Zhang, Y.; Zhu, J. Vapor phase nucleation and sedimentation of dispersed nanodiamonds by MPCVD. *Powder Technol.* **2024**, *436*, 119507. [[CrossRef](#)]
29. Bogdan, G.; De Corte, K.; Deferme, W.; Haenen, K.; Nesládek, M. Thick single crystal CVD diamond prepared from CH<sub>4</sub>-rich mixtures. *Phys. Status Sol.a* **2006**, *203*, 3063–3069. [[CrossRef](#)]
30. Tallaire, A.; Achard, J.; Silva, F.; Brinza, O.; Gicquel, A. Growth of large size diamond single crystals by plasma assisted chemical vapour deposition: Recent achievements and remaining challenges. *Comptes Rendus Phys.* **2013**, *14*, 169–184. [[CrossRef](#)]
31. Tallaire, A.; Mille, V.; Brinza, O.; Thi, T.N.T.; Brom, J.M.; Loguinov, Y.; Katrusha, A.; Koliadin, A.; Achard, J. Thick CVD diamond films grown on high-quality type IIa HPHT diamond substrates from New Diamond Technology. *Diamond Relat. Mater.* **2017**, *77*, 146–152. [[CrossRef](#)]
32. Yamada, H.; Chayahara, A.; Mokuno, Y. Method to increase the thickness and quality of diamond layers using plasma chemical vapor deposition under (H, C, N, O) system. *Diamond Relat. Mater.* **2020**, *101*, 107652. [[CrossRef](#)]
33. Osipov, V.Y.; Shames, A.I.; Enoki, T.; Takai, K.; Baidakova, M.V.; Vul, A.Y. Paramagnetic defects and exchange coupled spins in pristine ultrananocrystalline diamonds. *Diam. Relat. Mater.* **2007**, *16*, 2035–2038. [[CrossRef](#)]
34. Nagy, V.Y.; Komozin, P.N.; Desrosiers, M.F. Choosing reference samples for EPR concentration measurements. Part 3. Systems of S = 3/2. *Anal. Chim. Acta* **1997**, *339*, 31–51. [[CrossRef](#)]
35. Shames, A.I.; Osipov, V.Y.; Boudou, J.P.; Panich, A.M.; von Bardeleben, H.J.; Treussart, F.; Vul', A.Y. Magnetic resonance tracking of fluorescent nanodiamond fabrication. *J. Phys. D Appl. Phys.* **2015**, *48*, 155302. [[CrossRef](#)]
36. Stoll, S.; Schweiger, A. EasySpin, a comprehensive software package for spectral simulation and analysis in EPR. *J. Magn. Reson.* **2006**, *178*, 42–55. [[CrossRef](#)]
37. Breeding, C.M.; Shigley, J.E. The 'type' classification system of diamonds and its importance in gemology. *Gems Gemol.* **2009**, *45*, 96–111. [[CrossRef](#)]
38. Speich, L.; Kohn, S.C. QUIDDIT—Quantification of infrared active Defects in Diamond and Inferred Temperatures. *Comput. Geosci.* **2020**, *144*, 104558. [[CrossRef](#)]
39. Loubser, J.H.N.; van Wyk, J.A. Electron spin resonance in the study of diamond. *Rep. Prog. Phys.* **1978**, *41*, 1201–1248. [[CrossRef](#)]
40. Ammerlaan, C.A.J. *Impurities and Defects in Group IV Elements and III-V Compounds*; Springer: Berlin/Heidelberg, Germany, 1998; Volume 22, ISBN 978-3-540-48331-1.
41. Portis, A.M. Rapid Passage Effects in Electron Spin Resonance. *Phys. Rev.* **1955**, *100*, 1219–1221. [[CrossRef](#)]
42. Rovere, M.; Porro, S.; Musso, S.; Shames, A.I.; Williams, O.; Bruno, P.; Tagliaferro, A.; Gruen, D.M. Study of Detonation Nanodiamonds by Electron Paramagnetic Resonance. *Diamond Relat. Mater.* **2006**, *15*, 1913–1916. [[CrossRef](#)]
43. Casabianca, L.B.; Shames, A.I.; Panich, A.M.; Shenderova, O.; Frydman, L. Factors Affecting DNP NMR in Polycrystalline Diamond Samples. *J. Phys. Chem. C* **2011**, *115*, 19041–19048. [[CrossRef](#)]
44. Panich, A.M. Nuclear magnetic resonance studies of nanodiamonds. *Crit. Rev. Solid State Mater. Sci.* **2012**, *37*, 276–303. [[CrossRef](#)]
45. Shames, A.I.; Mogilyansky, D.; Panich, A.M.; Sergeev, N.A.; Olszewski, M.; Boudou, J.P.; Osipov, V.Y. XRD, NMR, and EPR study of polycrystalline micro- and nano-diamonds prepared by a shock wave compression method. *Phys. Status Solidi a* **2015**, *212*, 2400–2409. [[CrossRef](#)]
46. Panich, A.M.; Shames, A.I.; Mogilyansky, D.; Goren, S.D.; Dolmatov, V.Y. Detonation nanodiamonds fabricated from tetryl: Synthesis, NMR, EPR and XRD study. *Diamond Relat. Mater.* **2020**, *108*, 107918. [[CrossRef](#)]
47. Panich, A.M. Nuclear magnetic resonance studies of nanodiamond surface modification. *Diam. Relat. Mater.* **2017**, *79*, 21–31. [[CrossRef](#)]
48. Abragam, A. *The Principles of Nuclear Magnetism*; Clarendon Press: Oxford, UK, 1961.
49. Goldman, M. *Spin Temperature and Nuclear Magnetic Resonance in Solids*; Clarendon Press: Oxford, UK, 1970.
50. Shames, A.I.; Panich, A.M.; Kempinski, W.; Alexenskii, A.E.; Baidakova, M.V.; Dideikin, A.T.; Osipov, V.Y.; Siklitski, V.I.; Osawa, E.; Ozawa, M.; et al. Defects and impurities in nanodiamonds: EPR, NMR and TEM study. *J. Phys. Chem. Solids* **2002**, *63*, 1993–2001. [[CrossRef](#)]
51. Shames, A.I.; Panich, A.M.; Porro, S.; Rovere, M.; Musso, S.; Tagliaferro, A.; Baidakova, M.V.; Osipov, V.Y.; Vul', A.Y.; Enoki, T.; et al. Defects localization and nature in bulk and thin film ultrananocrystalline diamond. *Diam. Relat. Mater.* **2007**, *16*, 1806–1812. [[CrossRef](#)]
52. Panich, A.M. Universal Dependence of Nuclear Spin Relaxation on the Concentration of Paramagnetic Centers in Nano- and Microdiamonds. *Materials* **2022**, *15*, 5774. [[CrossRef](#)] [[PubMed](#)]
53. Shames, A.I.; Panich, A.M.; Friedlander, L.; Dolmatov, V.Y. Magnetic resonance study of novel detonation nanodiamonds originated from non-conventional explosives. *Diam. Relat. Mater.* **2023**, *136*, 110059. [[CrossRef](#)]
54. Mollart, T.P.; Lewis, K.L. The Infrared Optical Properties of CVD Diamond at Elevated Temperatures. *Phys. Status Sol. a* **2001**, *186*, 309–318. [[CrossRef](#)]
55. McNamara, K.M.; Gleason, K.K. Radial Distribution of Hydrogen in Chemical Vapor Deposited Diamond. *Chem. Mater.* **1994**, *6*, 39–43. [[CrossRef](#)]

56. Osipov, V.Y.; Shames, A.I.; Efimov, N.N.; Shakhov, F.M.; Kidalov, S.V.; Minin, V.V.; Vul', A.Y. Evolution of triplet paramagnetic centers in diamonds obtained by sintering of detonation nanodiamonds at high pressure and temperature. *Phys. Solid State* **2018**, *60*, 723–729. [[CrossRef](#)]
57. Nir-Arad, O.; Shlomi, D.H.; Manukovsky, N.; Laster, E.; Kaminker, I. Nitrogen Substitutions Aggregation and Clustering in Diamonds as Revealed by High-Field Electron Paramagnetic Resonance. *J. Am. Chem. Soc.* **2023**, *146*, 5100–5107. [[CrossRef](#)] [[PubMed](#)]
58. van Wyk, J.A.; Reynhardt, E.C.; High, G.L.; Kiflawi, I. The dependences of ESR line widths and spin-spin relaxation times of single nitrogen defects on the concentration of nitrogen defects in diamond. *J. Phys. D Appl. Phys.* **1997**, *30*, 1790–1793.
59. Nadolinny, V.A.; Shatsky, V.S.; Yuryeva, O.P.; Rakhmanova, M.I.; Komarovskikh, A.Y.; Kalinin, A.; Palyanov, Y.N. Formation features of N3V centers in diamonds from the Kholomolokh placer in the Northeast Siberian Craton. *Phys. Chem. Miner.* **2020**, *47*, 4. [[CrossRef](#)]
60. van Wyk, J.A.; Loubser, J.H.N. *Henderson*; Diamond Conference: Bristol, UK, 1980; p. 90.
61. Bloembergen, N. The interaction of nuclear spins in a crystalline lattice. *Physica* **1949**, *15*, 386–426. [[CrossRef](#)]
62. Reynhardt, E.C.; High, G.L. Nuclear magnetic resonance studies of diamond. *Prog. Nucl. Magn. Reson. Spectrosc.* **2001**, *38*, 37–81. [[CrossRef](#)]
63. Hoch, M.J.R.; Reynhardt, E.C. Nuclear spin-lattice relaxation of dilute spins in semiconducting diamond. *Phys. Rev. B* **1988**, *37*, 9222–9226. [[CrossRef](#)] [[PubMed](#)]

**Disclaimer/Publisher's Note:** The statements, opinions and data contained in all publications are solely those of the individual author(s) and contributor(s) and not of MDPI and/or the editor(s). MDPI and/or the editor(s) disclaim responsibility for any injury to people or property resulting from any ideas, methods, instructions or products referred to in the content.